Supplementary Materials for

Seismic evidence for Earth's crusty deep mantle

Daniel A Frost, Sebastian Rost, Edward J Garnero, and Mingming Li

Correspondence to: dafrost@berkeley.edu

Supplementary Text

This study employs array analyses of a scattered wave related to PKKP in order to map fine scale heterogeneities in Earth's lowermost mantle. We use 14 small aperture seismic arrays of which 6 are equipped with broadband sensors, and 8 are dominantly short period sensors (Table S1). They range in aperture from 4 to 31 km and have between 16 and 28 sensor elements, making them ideal for studying the directional characteristics of scattered seismic waves.

Data collection

We collect vertical component recordings of events received at these 14 arrays. We select events within 60 degrees for the array with magnitudes above 6.0 as reported in the Reviewed Events Bulletin (REB) (Engdahl and Gunst, 1966). For the 13 International Monitoring System (IMS) arrays, we collect events from 1995 to 2012, while for Gauribidanur, we collect events from 1985 to 1996.

Distribution of scattering heterogeneity

We detect scattering heterogeneities within the lowermost mantle. The resolved distribution of scattering heterogeneities is partly a function of the sampling of the Earth by the available sources and receivers (Fig. 3e). We account for the variability in sampling to reveal the uneven distribution of heterogeneities throughout the lower mantle (Fig. S1). We find scattering heterogeneities to be more common in the northwestern Pacific, northwestern Atlantic, eastern Africa, off the coast of Central America, the Indian Ocean, and, in particular, southeastern Africa.

Comparison of scattering heterogeneity and structures in tomography

We explore the relationship between large-scale mantle structure and seismic scattering by comparing our resolved locations of scattering heterogeneities to S-wave tomography models and P-wave models (Fig. S2). Low seismic velocities define the LLVPs and are often more pronounced towards the centre of the LLVPs, while strong lateral velocity gradients are commonly located near the margins of LLVPs (Thorne et al., 2004). For each model, we calculate lateral velocity gradients ($\nabla(dVs)$) measured over a horizontal distance of 10°. The various tomographic models, especially shear wave models, present similar structures at large scales but significant differences are present for smaller length scales. The velocity gradients display more variability between models than velocities, and even more so for the P-wave models. However, larger scale patterns are broadly similar. We compare our mapped scattering heterogeneities to different tomographically derived velocities and gradients to establish if observed patterns depend upon specific models.

We seek to compare scattering heterogeneity locations to strength of lowermost mantle velocity anomalies and gradients for the models of Fig. S2. The different tomographic models vary in magnitude of the velocity perturbations, thus we pursue our correlative analysis by considering percentages of highest and lowest velocity anomalies and gradients as a function of cumulative CMB area, displayed in the right two columns of Fig. S2. In what follows we consider the tomographic velocity and gradient distributions by area (according to anomaly strength, as just discussed), and count our mapped scattering heterogeneities according to the area level. In Figure 8, we display a composite of the spatial relationship between scattering heterogeneities and the low velocities and high gradients from all 7 tomographic models considered, as a function of cumulative area. For example, for the comparison of scattering heterogeneities to the highest velocity anomalies, the horizontal axis ranges from small areas (on the left part of the plots) containing the very highest velocities, to then gradually larger and larger areas which include decreasing velocity amplitudes (towards the right of the plots). This measure is not influenced by the actual magnitude of velocity anomalies, and thus similarly assesses agreement of scattering locations to tomographic models containing different heterogeneity amplitudes. Figs. S3 and S4 display the relationship between scattering heterogeneities and high gradients, low gradients, high velocities, and low velocities, and also the relationship between scattering heterogeneities and randomly rotated tomographic models, for all 7 models individually. The grand mean and pooled variance (displayed in Figure 8) are calculated from the individual relationships shown here.

Overall, despite variation between models, we find that scattering heterogeneities are preferentially located in regions of the highest gradients and moderately low velocities, and show either no preference or an aversion to low gradients and higher velocities.

In Figures 9a and 9b in the main text, we display the spatial relationship between scattering heterogeneities and the velocity anomalies in tomographic model S40RTS (Ritsema et al., 2011) along a cross section from 140° W, 0° N to 70° E, 0° N. In Fig. S5 we display 4 different cross sections that demonstrate that scattering heterogeneities show an affinity for LLVP edges at a range of latitudes.

In Figures 9c and 9d in the main text, we show a single snapshot from a dynamic calculation of the interaction between oceanic crust, ambient mantle, and thermochemical piles (Li et al., 2014) using a non-compressible, Newtonian, fully Boussinesq calculation (Moresi and Gurnis, 1996). The distribution of crust and piles evolve as the model runs in time. The time parameter of the model is non-dimensional and is measured in time steps. The model runs for 120,000 steps, and, from initiation of subduction, the crust takes roughly 11,000 time steps to reach the CMB. We display a selected part of the evolution of the model at four more time steps (Fig. S6): 80,000, 82,000, 84,000, and 86,000. At all of these time steps, the oceanic crust is most prevalent near the edges of the thermochemical piles.

To complement the analysis of the lateral distribution of scattering heterogeneities, the depth distribution of scattering heterogeneities is compared to tomographic velocity anomalies (Fig. S7) and gradients (Fig. S8). We consider the mapped scattering heterogeneities in 50 km thick depth shells and associate them with tomographically derived velocity anomalies and gradients sorted by magnitude in bins of 20% CMB area. For example, in the first column in Fig. S7a, the darkest blue region represents the proportion of scattering heterogeneities in a region covering 20% of the CMB's area, which contains the highest velocity anomalies. We remove sampling bias by dividing the number of scattering heterogeneities in each 20% area bin (as a proportion of the total scattering population), by the potential sampling in the same area (as a proportion of the total sampling population) computed from our sampling coverage. The dark blue parts of the plot can be compared to the dark red parts (the latter corresponding to the lowest velocities in a 20% CMB area), which show that significantly more scatterers are in lowest velocity regions than in highest velocity regions. This comparison is shown for 7 different S-wave velocity tomography models and for 4 P-wave models. We find that, as was shown in Figs. S3 and S4, scattering heterogeneities are most common in regions with moderately low velocities and high gradients. The relationship between scattering heterogeneities and tomographically derived velocities remains fairly constant with height, however, 5 of the 7 models show an increase in the proportion of scattering heterogeneities in regions of high gradients with increasing height off the CMB.

Supplementary References:

Engdahl, E.R. and R.H. Gunst, 1966. Use of a high speed computer for the preliminary determination of earthquake hypocenters, *Bull. Seism. Soc. Am.*, 56, 325-336.

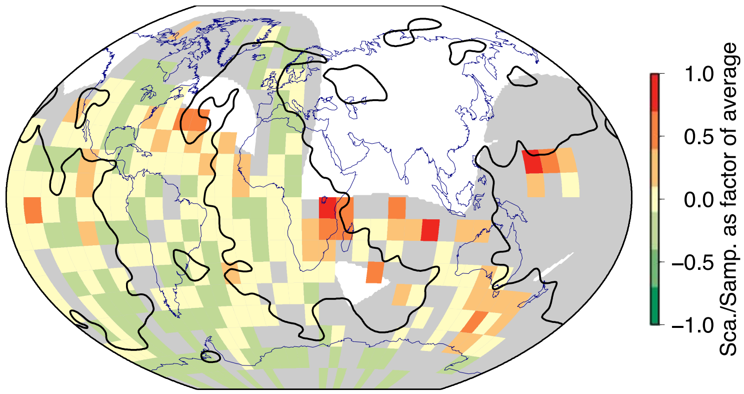

Fig. S1. Scattering heterogeneities normalised by sampling. Scattering count per 10° cell divided by the number of source-receiver pairs (Fig. 1d) sampling the same 10° cell. Ratio of scattering to sampling is rescaled to set the average to 0, thus 1 and -1 represent more and less scattering than average, respectively. Grey shading marks the extent of the sampled region, hence areas where coloured cells are absent are sampled but do not display scattering, while white regions are unsampled by this dataset. Black contours mark 0% dVs in the tomography model S40RTS (Ritsema et al., 2011).

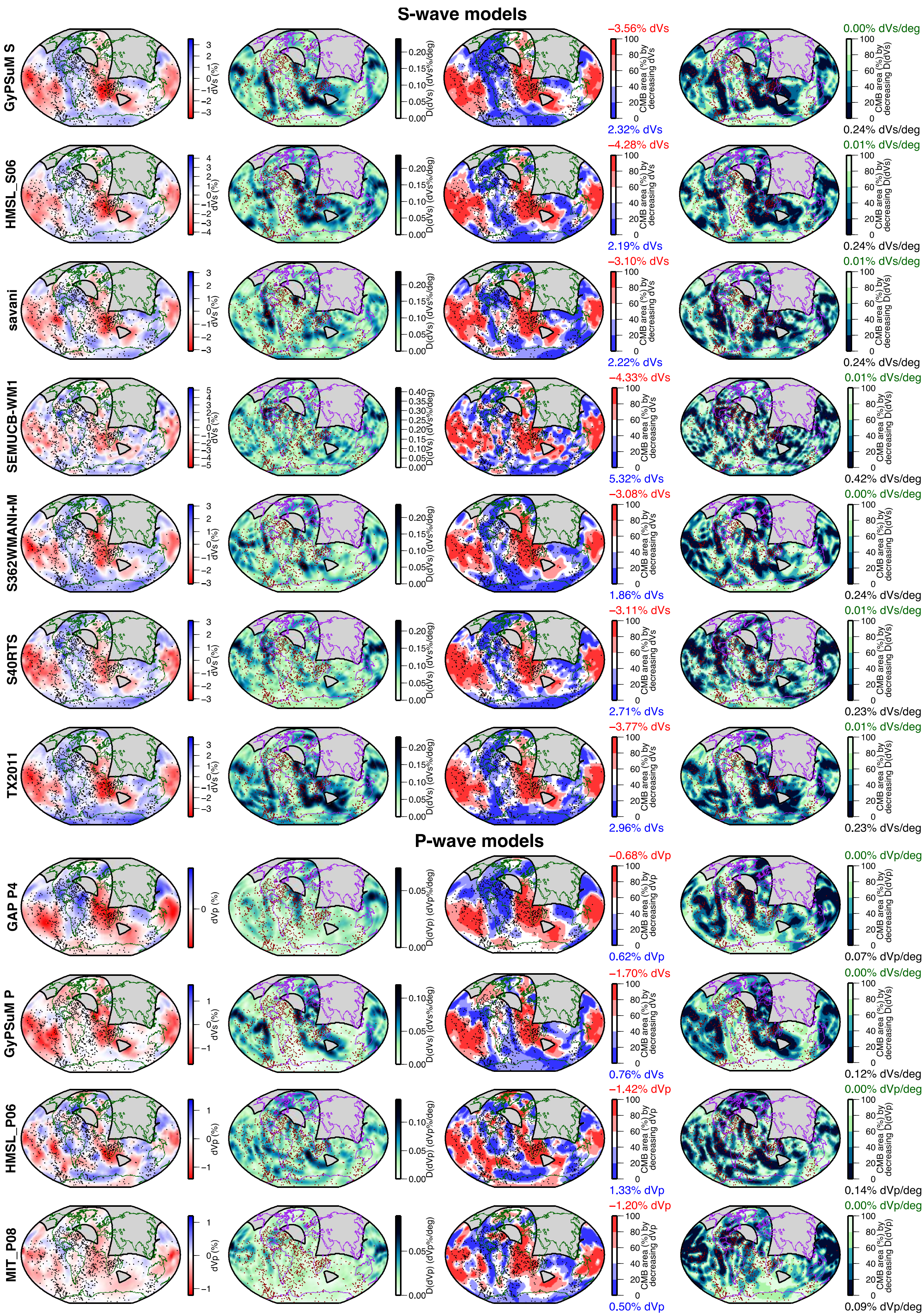
S-wave models
GyPSuM S
HMSL_S06
savani
SEMUCB-WM1
S362WMANI+M
S40RTS
TX2011
P-wave models
GAP P4
GyPSuM P
HMSL_P06
MIT_P08

Fig. S2. Scattering heterogeneities overlain on velocity anomalies and lateral velocity anomaly gradients in the lowermost depth slice of S-wave and P-wave tomography models. The left two columns display scattering heterogeneities (circles) plotted over velocity anomalies and lateral velocity gradients, respectively, in S-wave models GyPSuM (Simmons et al., 2010), HMSL-S06 (Houser et al., 2008), savani (Auer et al., 2014), SEMUCB-WM1 (French and Romanowicz, 2015), S362WMANI+M (Moulik and Ekstrom, 2014), S40RTS (Ritsema et al., 2011), and TX2011 (Grand, 2002) and P-wave models GAP_P4 (Obayashi et al., 2013), GyPSuM_P (Simmons et al., 2010), HMSL_P06 (Houser et al., 2008), and MIT-P08 (Li et al., 2008). The regions occupying 10% of the CMB's area that contains the lowest and highest dVs and dVp values are marked by red and blue contours, respectively, while the regions occupying 10% of the CMB's area that contains the lowest and highest dVs and dVp gradients are marked by green and purple contours, respectively. The right two columns display scattering heterogeneities plotted over velocity anomalies and lateral velocity gradients scaled by CMB area. Velocities are sorted by increasing velocity anomaly while gradients are sorted by decreasing lateral velocity gradient. Extremes of dVs and ∇(dVs) values for each model are displayed at the ends of the scale bar.

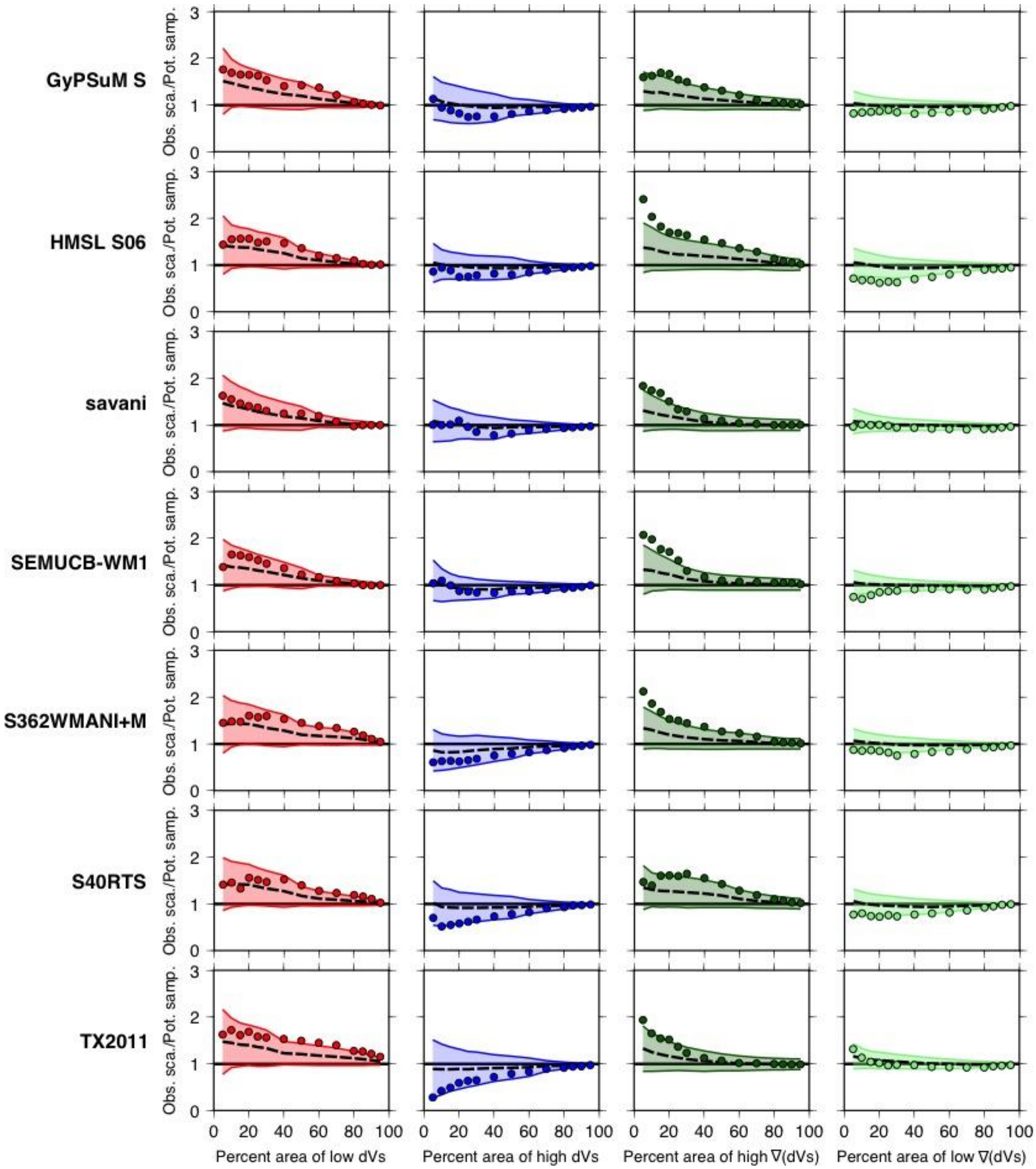

Fig. S3. Correlation between scattering heterogeneities and large-scale tomographic structure. Ratio of observed-to-potential percentage of scatterers measured in areas of low and high velocity perturbations (first and second columns) and strong and weak lateral velocity gradients (third and fourth columns), for the seven S-wave tomography models shown in Fig. S2. These ratios are compared to percentage of cumulative CMB area sorted by high or low velocity anomalies or gradients (e.g. 5% area of low dVs means the 5% of the CMB area that contains the lowest dVs values for that model). The relationship of our mapped scattering heterogeneity locations and tomographically derived velocities or gradients is marked by circles, which display the ratio of scattering heterogeneities to the sampling (as a proportion of the total heterogeneity and sampling population, respectively) within that CMB area. Ratios are calculated at a range of CMB areas: 5, 10, 15, 20, 25, 30, 40, 50, 60, 70, 80, 85, 90, and 95%. The ratio for 100% CMB area is 1. The tomography model is then randomly rotated 100 times and the correlation between the heterogeneities and the rotated model is calculated. The mean of the correlation for the randomly rotated models is shown by the dashed line, while one standard deviation about mean is shown by the shaded regions. A one-to-one correlation, where the percentage of scatterers observed is the same as that expected, is displayed by the black horizontal line (at the y-axis value of 1). Circles plotting above or below the black line indicate a greater or lesser abundance of scattering heterogeneities in that region of the model, respectively, than expected based on the concentration of sampling. Meanwhile, circles plotting outside of the shaded region indicate that the real data is different from at least 68% of the rotated models. This suggests that the correlation with the tomography model is less likely a result of a chance similarity between the data and the model, and so the result is likely statistically significant.

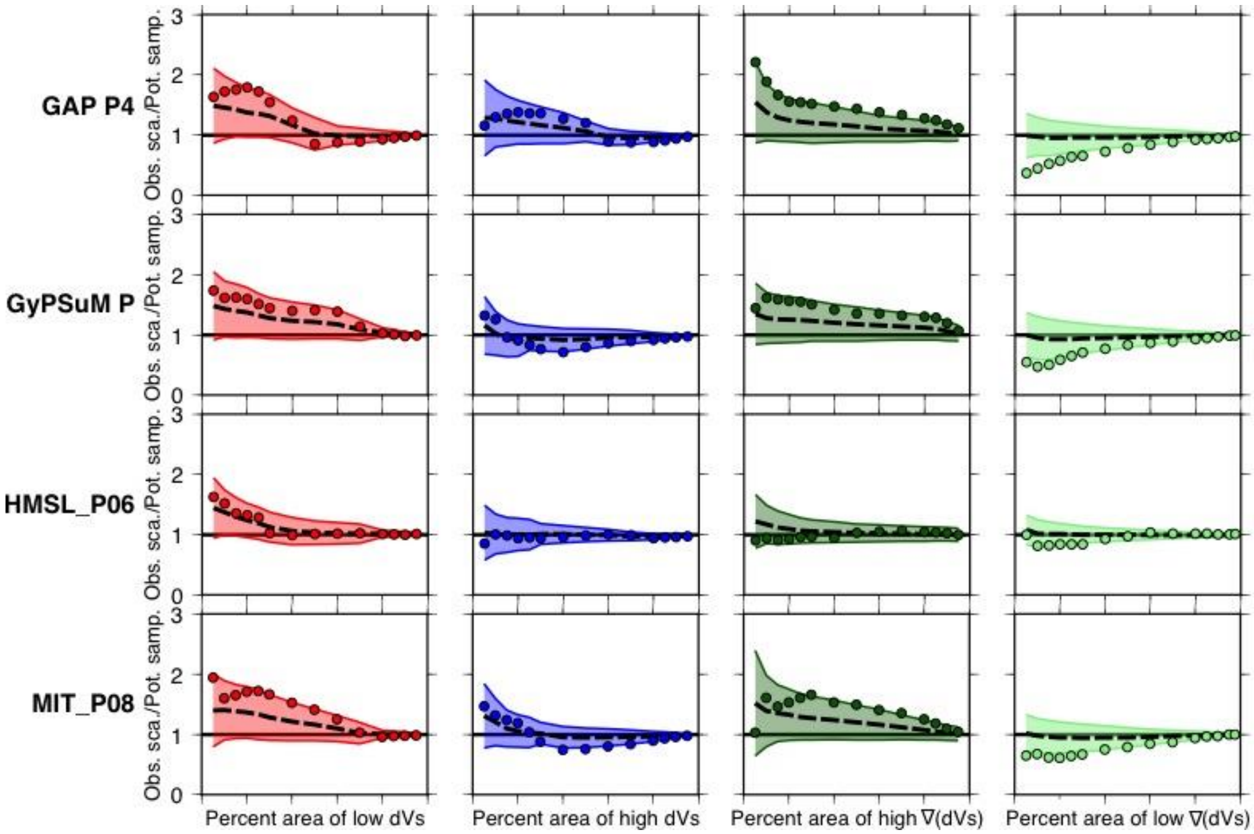

Fig. S4. Correlation between scattering heterogeneities and large-scale tomographic structure. Ratio of observed-to-potential percentage of scatterers measured in areas of low and high velocity perturbations (first and second columns) and strong and weak lateral velocity gradients (third and fourth columns), for the four P-wave tomography models shown in Fig. S2. Lines and shading as in Fig. S3.

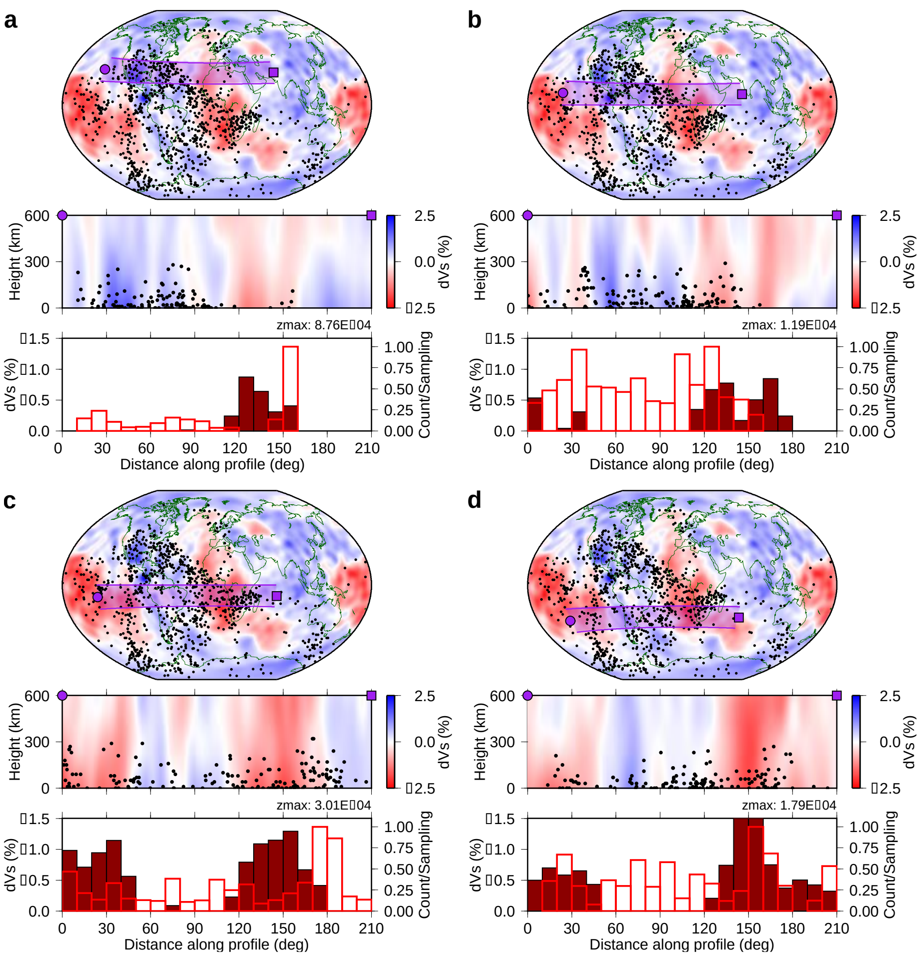

Fig. S5. Cross-sections displaying distribution of observed scattering heterogeneities. Cross-sections, as in Figure 8 of the main text, compare scattering to tomography velocities from S40RTS (Ritsema et al., 2011). All cross-sections are from -140 W (purple circle) to 70 E (purple square), thus 210 degrees longitude the in the east-west direction, along different latitudes: **(a)** latitude = 30 N, **(b)** latitude = 10 N, **(c)** latitude = 10 S, and **(d)** latitude = 30 S. The top panel for each part displays a map showing dVs of the tomographic model S40RTS at 2889 km depth, along with our mapped scattering heterogeneities. A 20 degree wide swath (purple region) is used to assess comparisons between scatterers and heterogeneity in the lower two parts of each figure part. The middle panel shows the tomography model S40RTS in the lowest 600 km of the mantle, averaged across the cross-section swaths, along with our imaged scattering heterogeneity locations (black dots) in lowermost 320 km of mantle. The lowermost panel presents the ratio of observed to potential scattering heterogeneities along the cross-section swath in open red bars (the ratio, normalised to one, is displayed on the vertical axis on the right side, while the maximum of the ratio is shown at the top right corner of the histogram). The amplitude of LLVP dVs averaged in 10 degree intervals along the cross-section and across the swath are also shown by the filled dark red bars (values are plotted on the left vertical axis).

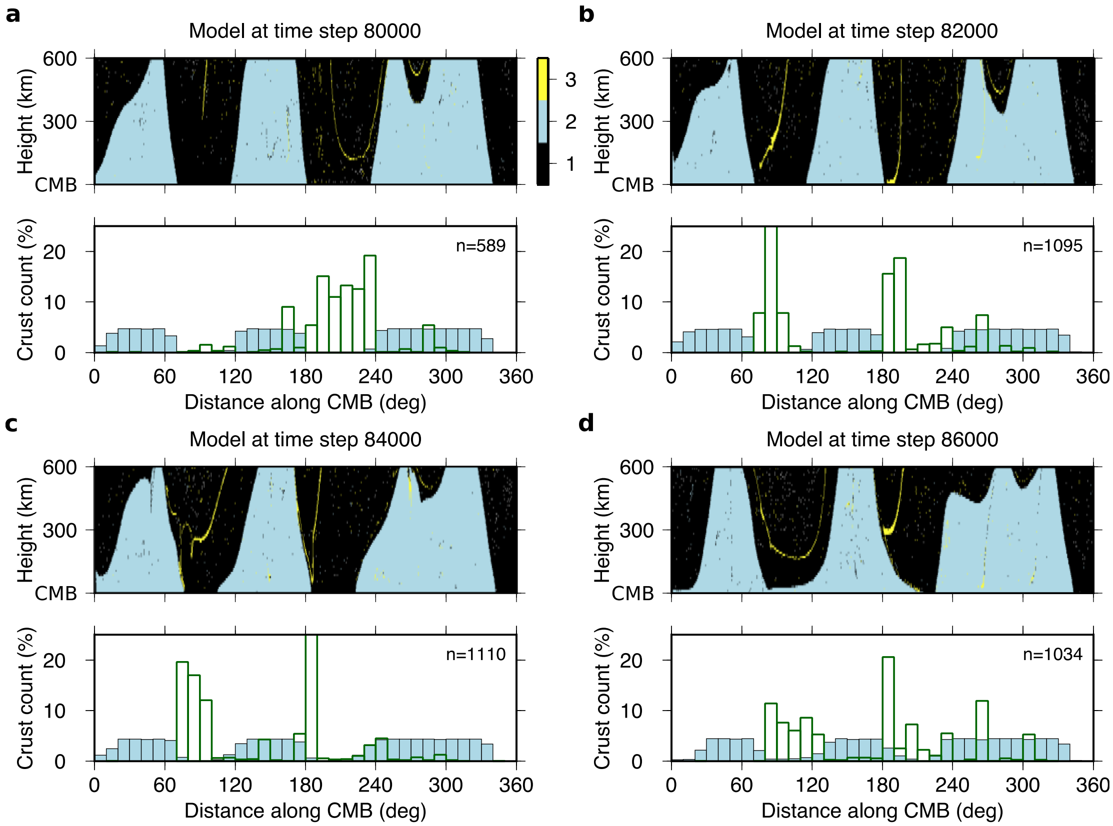

Fig. S6. Multiple time steps from numerical convection showing evolution of mantle heterogeneities. Numerical convection calculations, as in Figure 9 of the main text, display the interaction between subducting oceanic crust tracers (yellow), dense thermochemical piles (blue), and the ambient background mantle (black). The evolution of the calculation is shown for 3 time steps: **(a)** 80000, **(b)** 82000, **(c)** 84000, and **(d)** 86000. The upper panel of each time-step is a cross-section in the convection calculation showing tracers representing the three types of chemistry (mantle, pile, crust) in the calculation. The tracers are displayed in 10 by 10 km cells coloured by the most prevalent tracer type. The lower panel of each time-step displays the lateral distribution of oceanic crustal material tracers (green open bars) and pile material tracers (blue-filled bars) in the lowermost 300 km of the mantle. Subducting crust that encounters thermochemical pile edges then is upwardly entrained at pile edge locations, accounting for an increase in crustal tracers there.

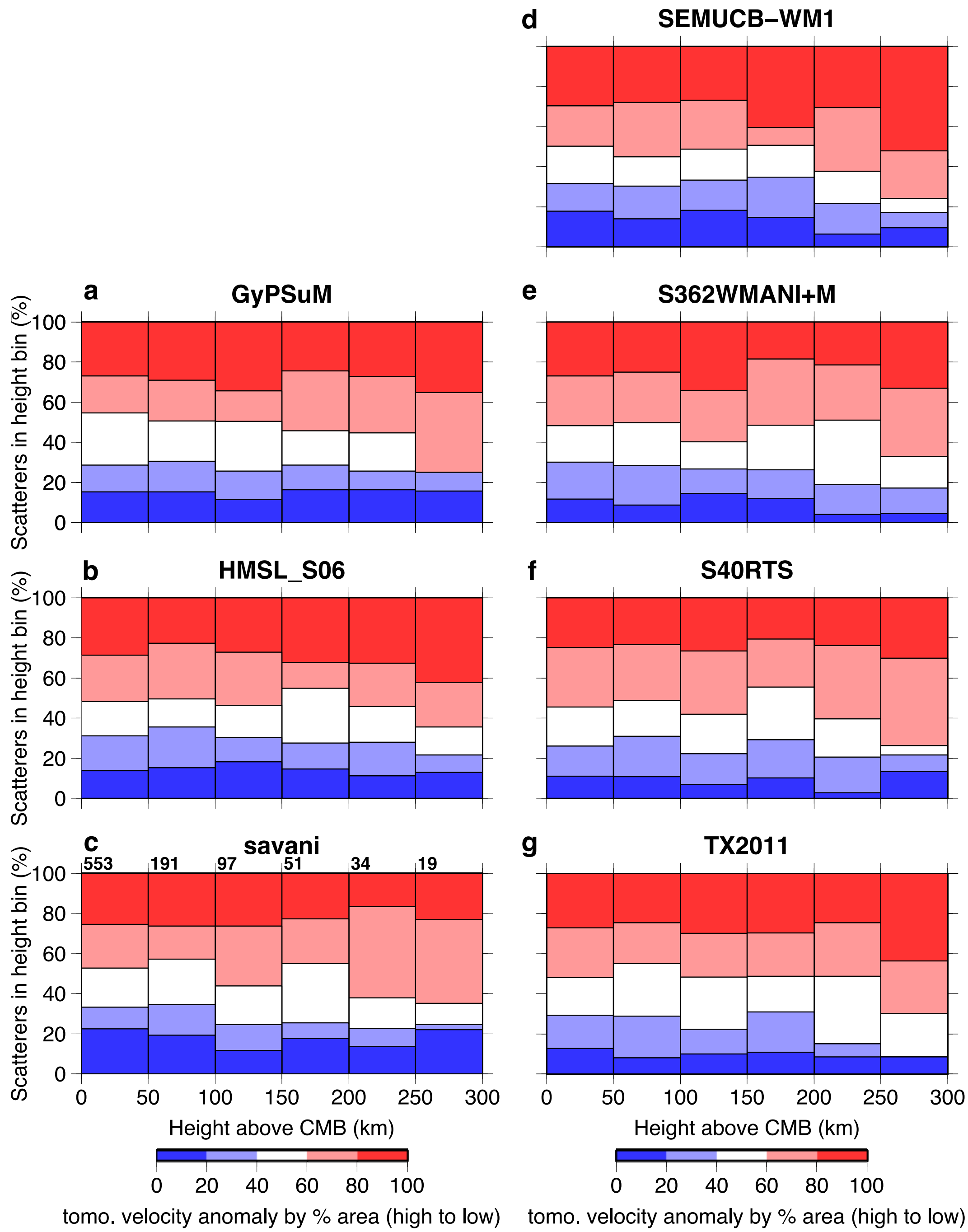

Fig. S7. Proportion of scattering heterogeneities by height above the CMB for different velocity models. Within each height range, scattering heterogeneities are spatially associated with regions of high to low tomographic velocity anomalies in 20 % CMB area groups for models **(a)** GyPSuM, **(b)** HMSL-S06, **(c)** savani, **(d)** SEMUCB-WM1, **(e)** S362WMANI+M, **(f)** S40RTS, **(g)** TX2011. The percentage of heterogeneities (as a proportion of the total in that height range) in each velocity anomaly region is weighted by percentage of samples in the same region (as a proportion of the total in that height range (see Figure 3e). The weighting removes the bias that good/poor sampling would introduce when counting heterogeneities. The absolute number of heterogeneities within each height layer is displayed above each column in c). The calculation is repeated for each of the 7 S-wave tomography models used in the study. For all models, the highest 40% of velocity anomalies typically contain fewer than 30% of the scattering heterogeneities. Meanwhile, also for all models, the lowest 40% of velocity anomalies contain the greater than 50% of the scattering heterogeneities, and this association becomes stronger for scattering higher above the CMB.

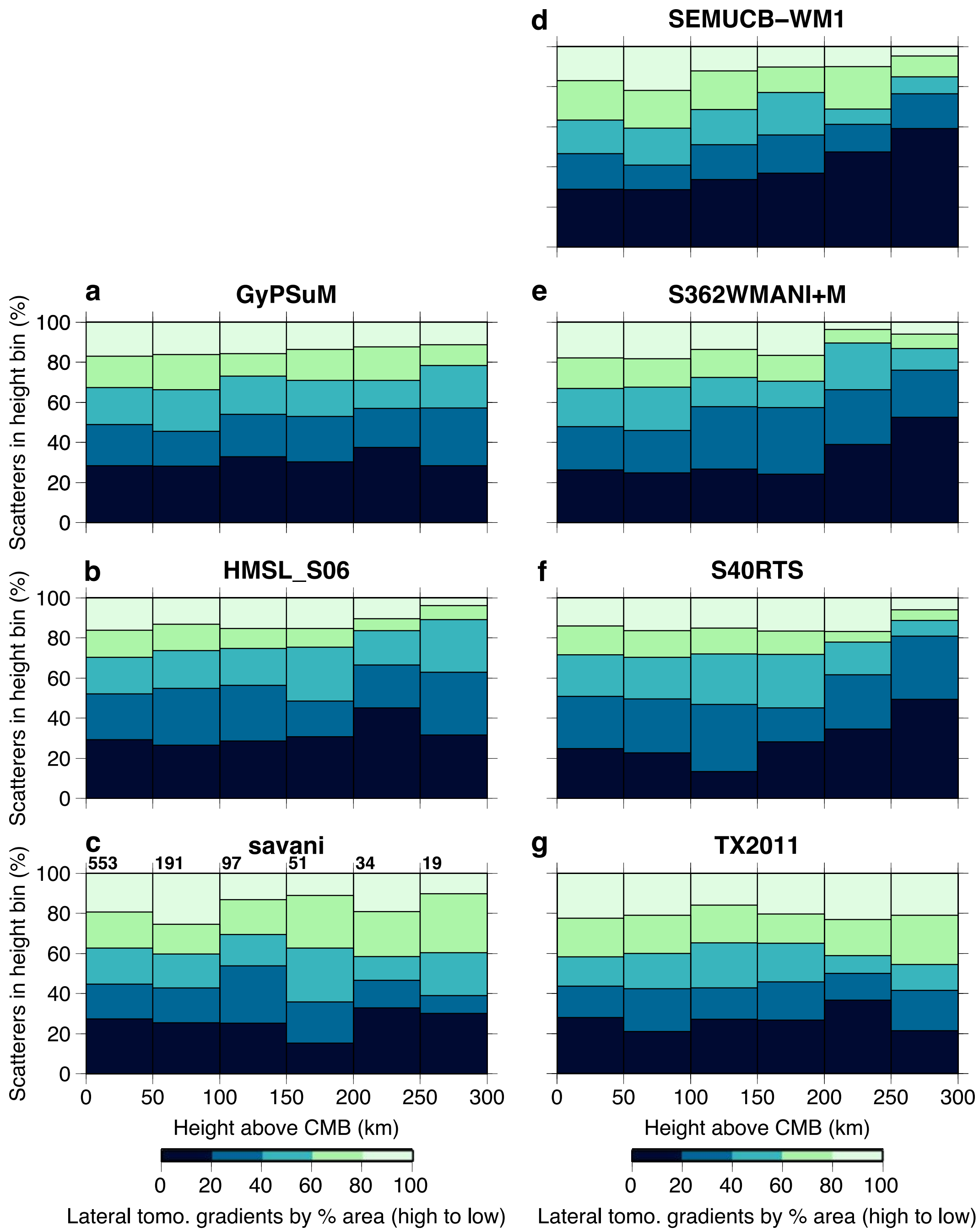

Fig. S8. Proportion of scattering heterogeneities by lateral velocity anomaly gradient for various heights above the CMB. Within each height range, scattering heterogeneities are spatially associated with regions of strong to weak lateral velocity anomaly gradients in 20 % CMB area groups **(a)** GyPSuM, **(b)** HMSL-S06, **(c)** savani, **(d)** SEMUCB-WM1, **(e)** S362WMANI+M, **(f)** S40RTS, **(g)** TX2011. The percentage of heterogeneities (as a proportion of the total in that height range) in each velocity anomaly region is weighted by percentage of samples in the same region (as a proportion of the total in that height range (see Figure 3e). The weighting removes the bias that good/poor sampling would introduce when counting heterogeneities. The absolute number of heterogeneities within each height layer is displayed above each panel in c). The calculation is repeated for each of the 7 S-wave tomography models used in the study. The weakest 40% of velocity gradient anomalies typically contain around 30% of the scattering heterogeneities. In contrast, the strongest 40% of velocity anomaly gradients contain 40 to 50% of scattering heterogeneities, and, for all models, except TX2011 and savani, this association becomes stronger for scattering higher above the CMB.

Table S1. Characteristics of arrays used in study.

Array Name	Location	Array Code	Latitude (deg)	Longitude (deg)	Number of stations	Aperture (km)	Average Station spacing (km)	Sensor type
Malin	Ukraine	AK	50.70	29.22	24	27.6	3.2	Broad-band
Alice Springs	Australia	AS	-23.67	133.91	19	10.0	1.7	Short period
Chiang Mai	Thailand	CM	18.46	98.94	18	10.1	2.0	Short period
Eskdalemuir	Scotland	EK	55.33	-3.16	20	8.6	0.8	Broad-band
Sonseca	Spain	ES	39.67	-3.96	28	38.2	4.3	Broad-band
Gauribidanur	India	GB	13.60	77.44	25	30.8	2.2	Short period
GERESS	Germany	GE	48.85	13.70	19	3.9	0.3	Short period
Eilson	USA	IL	64.77	-146.89	21	10.2	1.4	Short period
Wonju	Korea	KS	37.44	127.88	20	10.1	1.8	Short period
Kurchatov	Kazakh-stan	KU	50.62	78.53	21	22.5	2.2	Broad-band
Matsushiro	Japan	MJ	36.52	138.25	23	11.2	0.8	Short period
Torodi	Niger	TO	13.15	1.69	16	6.1	1.2	Broad-band
Warramunga	Australia	WR	-19.94	134.34	24	26.3	1.8	Broad-band
Yellowknife	Canada	YK	62.49	-114.61	18	22.7	2.5	Short period